ACS APPLIED MATERIALS & INTERFACES

www.acsami.org

Research Article

Unraveling Impurity-Dependent Morphological and Chemical Evolution of Ni−20Cr Alloy in Eutectic LiCl−KCl Molten Salt

Yuxiang Peng,* Kaustubh K. Bawane, Xiaoyang Liu, Xiaoyin Zheng, Mingyuan Ge, Xianghui Xiao, Ellie M. Kim, Phillip W. Halstenberg, Sheng Dai, James F. Wishart, and Yu-chen Karen Chen-Wiegart*

Cite This: *ACS Appl. Mater. Interfaces* 2025, 17, 28764−28776

Read Online

ACCESS | Metrics & More | Article Recommendations | Supporting Information

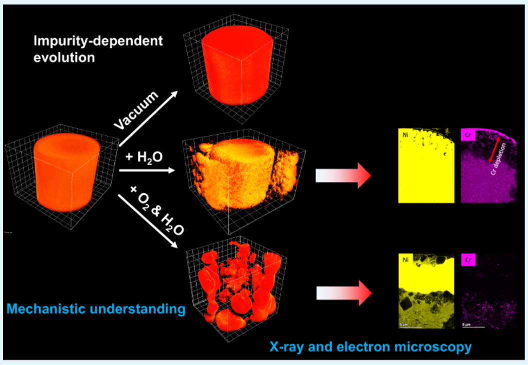

ABSTRACT: Understanding the interfacial evolution of alloys in molten salt with different amounts of water (H_2O) and oxygen (O_2) impurities is significant for applications in many fields, including concentrated solar power, molten salt reactors, and applications in pyrochemical reprocessing and electrorefining. Additionally, the impurity-driven corrosion mechanisms that lead to various morphological and chemical evolution characteristics at the interfaces of structural alloys and molten salts are not fully understood. In the present work, the three-dimensional (3D) morphological evolution of Ni−20Cr microwires in LiCl−KCl was studied at 500 °C under different moisture and oxygen conditions using in situ synchrotron transmission X-ray microscopy (TXM) and scanning transmission electron microscopy (STEM) techniques. No significant morphological changes were observed in Ni−20Cr microwires under vacuum conditions. However, the wires exhibited distinct morphological evolutions when exposed to molten salt containing H_2O alone, as well as when both H_2O and O_2 were present. Furthermore, Cr_2O_3 precipitates were observed in the molten salt during corrosion with only H_2O present, while Cr^{6+} species were identified in the salt when O_2 was added. These findings are crucial for understanding the corrosion mechanisms of molten salt with different amounts of H_2O and O_2 contamination, providing insights for developing corrosion mitigation methods and improving the stability of containment alloys in molten salt applications.

KEYWORDS: *LiCl-KCl, TXM, STEM, Ni−20Cr, impurities, corrosion*

1. INTRODUCTION

Over the past decade, molten chloride salts have been attractive in many applications as promising coolant candidates in concentrated solar power (CSP) systems[1,2] and molten salt reactors (MSR),[3,4] owing to their desirable thermal properties, such as low cost, large heat capacity, high thermal conductivity, low melting point,[5] and high thermal stability.[6] In MSR, they are also employed as fuel salt due to their good neutronic properties,[7] which can enhance fuel efficiency and utilization.[8,9]

LiCl−KCl eutectic salt is used in many applications because of its relatively low melting point (353 °C)[10] and chemical stability. In addition, it has been widely used in pyrochemical reprocessing and electrorefining applications.[10−12] However, the use of molten chloride salts remains limited due to the corrosion of containers and structural alloys.[13−15] Ni−Cr based alloys are chosen to be structural materials in high-temperature applications because Ni has been proven to be stable in molten chloride salt.[16] A minimum of 15 wt % Cr is required for the Ni-based alloy to enhance high-temperature corrosion resistance in air.[17] The redox potentials of chloride salts, like KCl/K, are lower than that of $CrCl_3$/Cr, $CrCl_2$/Cr, and $NiCl_2$/Ni,[3] and thus Ni−Cr based alloys are in theory thermodynamically stable in the pure molten chloride salt. However, it is commonly acknowledged that the corrosion process is driven by impurities such as H_2O and O_2.[14,15,18,19] Impure molten salt results in higher corrosion rates of structural alloys as discussed in a recent review.[20] According to their respective redox potentials, Cr will be corroded preferentially over Ni in the Ni−Cr based alloys. However, the increased number of impurities will further induce the corrosion of the Ni element.[21,22]

The impurities are mainly from water and O_2-dissolved compounds in the chloride salt, as well as in the atmosphere.[23] In addition, moisture in the salt is usually in the form of hydrates. In LiCl−KCl salt system, LiCl has a strong tendency to absorb water from the atmosphere and form lithium chloride monohydrate, $LiCl{\cdot}H_2O$.[24] During the heating process, the hydrated salt will produce oxide, hydroxide

Received: December 31, 2024
Revised: April 7, 2025
Accepted: April 8, 2025
Published: April 29, 2025

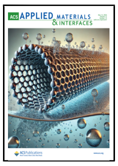

https://doi.org/10.1021/acsami.4c23034
ACS Appl. Mater. Interfaces 2025, 17, 28764−28776

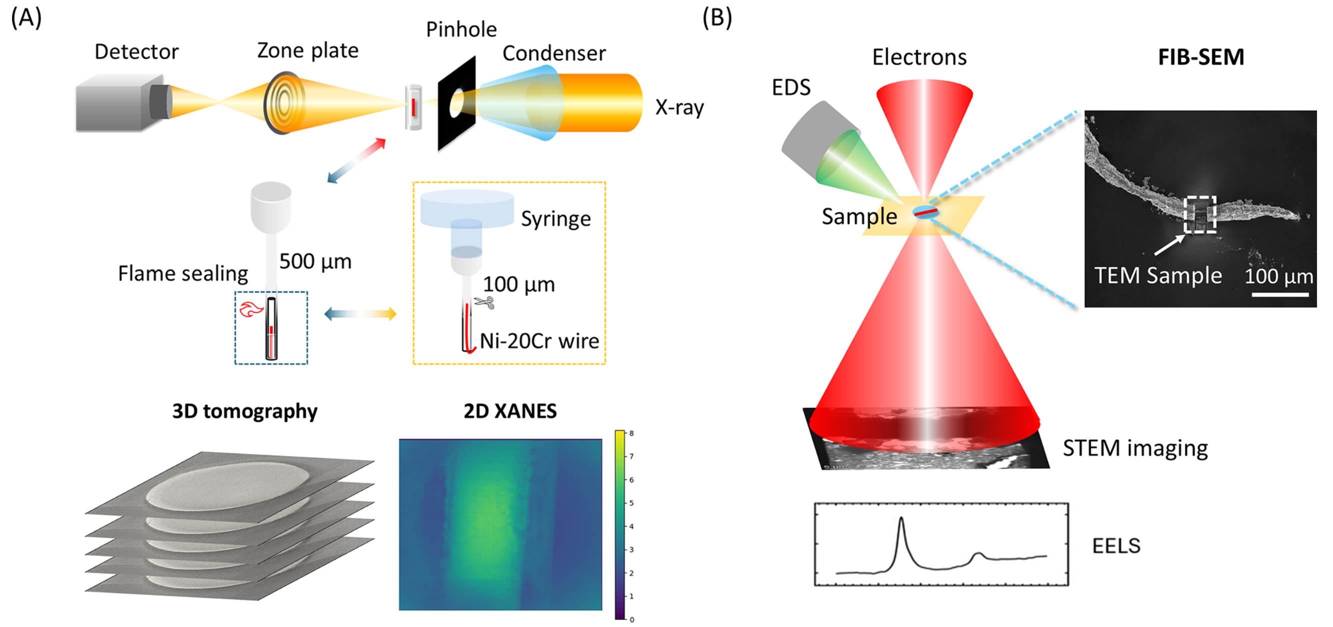

Figure 1. Experimental setup and sample preparation method of an in situ synchrotron transmission X-ray microscope (TXM) and scanning transmission electron microscopy (STEM). (A) In-situ TXM setup. (B) Post-TXM analysis: a focused ion beam-scanning electron microscope (FIB-SEM) system is used for extracting the sample, followed by analysis with an STEM coupled with energy-dispersive X-ray spectroscopy (EDS) and electron energy loss spectroscopy (EELS).

compounds, and hydrogen chloride gas, which will be reactive toward the structural alloys.[25] Although it is well known that impurities will influence the corrosion process, the corrosion mechanisms with different amounts of impurities have not been discussed in depth, in part due to the challenge in controlling the kind and quantity of impurities in the system and in part due to the difficulty of characterizing the intermediate changes in morphology and corrosion products.

The synchrotron transmission X-ray microscope (TXM) technique has been used to characterize the morphological evolution of alloys in molten salt[13,22,26] as it enables direct 3D imaging of a wide range of materials. In addition, since the morphological evolution can be captured as a function of time, the material kinetics, including pathways and rates, can be quantified.[27,28] Therefore, the changes in material interfaces in molten salt, such as coarsening,[21] dissolution, changing in pore/ligament network,[22] and precipitate formation with time, can be captured and quantified. Furthermore, chemical information and phase changes can be detected using spectroscopic imaging with TXM, via X-ray absorption near-edge structure (XANES) spectroscopy.[29,30]

In this work, the Ni−20Cr alloy was selected as a model to investigate the corrosion behavior of Ni−Cr based alloys in a common molten salt. Corrosion of Ni−20Cr alloy in molten LiCl−KCl (59.2−41.8 mol %) at 500 °C with different amounts of water and oxygen content in the atmosphere was studied by in situ synchrotron TXM. We choose 500 °C because it is within the operational temperature range for MSRs,[4] and the moderate rate of corrosion compared to higher temperatures allows for more precise characterization of morphological changes using in situ techniques with appropriate time resolution. For further analysis, the in situ samples after corrosion were preserved without exposure to air and moisture and analyzed by scanning transmission electron microscopy (STEM) coupled with energy-dispersive X-ray spectroscopy (EDS) and electron energy loss spectroscopy (EELS). Through observation and analysis of the morphological evolution and chemical changes at different times and length scales, a general corrosion mechanism for the Ni−20Cr alloy in LiCl−KCl molten salt with different amounts of impurities was proposed.

2. EXPERIMENTAL DETAILS

2.1. Materials. A eutectic LiCl and KCl mixture (59.2:41.8 mol %) was used as the solvent in the present study. LiCl was further purified via sparging with Cl_2 gas at 800 °C.[31,32] After chlorination, LiCl was transported into an Ar-filled glovebox for storage. KCl was purchased as 99.999% AnhydroBeads 10 mesh from Sigma-Aldrich. KCl was dehydrated at 500 °C under vacuum for 2 h and then transported to the glovebox. The LiCl and KCl were weighed in a eutectic ratio and then fused together under vacuum. Ni−20Cr (80 wt % Ni − 20 wt % Cr) microwires with 20 μm in diameter (99.5% pure) were purchased from Goodfellow.

2.2. Experimental Procedure of In Situ Synchrotron TXM. Sample preparation for the experiment of full field X-ray Imaging beamline (FXI, 18-ID)[33] at the National Synchrotron Light Source-II (NSLS-II), Brookhaven National Laboratory (BNL), was conducted following a procedure established in our prior work[34] with modifications to introduce different extent of impurities. Approximately 1.0 g of eutectic LiCl-KCl salt was melted in a quartz boat at 550 °C in an argon-filled glovebox. Prior to the sample preparation, all the capillaries were baked at 500 °C for 2 h to remove the organic residues and adsorbed moisture. The schematic of the FXI beamline with the sealed double-capillary sample preparation is shown in Figure 1(A).

Sealed double-quartz capillary samples containing Ni−20Cr microwire and solidified LiCl-KCl salt were prepared in the argon-filled glovebox following the established protocol.[21] Briefly, the Ni−20Cr microwire and salt were placed into a 100 μm diameter open-ended quartz capillary (Charles Supper, 01-

QZ), which was then inserted into a larger outer quartz capillary (Charles Supper, 05-QZ) of 500 μm diameter.

Subsequently, three types of samples were prepared: 1) sample sealed under vacuum (sample−vacuum); 2) sample sealed with moisture (sample−moisture); and 3) sample sealed under room air (sample−air). For the sample−vacuum, the open-end of the 500 μm quartz capillary was attached to a Swagelok fitting with a closed valve and transferred to the glovebox. The other end of the Swagelok fitting was then connected to a mechanical vacuum pump and pumped for ∼5 min before flame sealing. For the sample−moisture, the funnel side of the capillary was sealed with epoxy and cured overnight in a glovebox and then transferred out of the glovebox for flame sealing. Water evolution is common in epoxy resin,[35,36] which will be more severe in the commercial epoxy, and the water uptake is 2−3 wt %.[37] Therefore, the amount of water can be calculated based on the vapor pressure of water at 298 K, which is 0.03 atm.[38] The content of gas sealed in the quartz capillary is estimated to be ∼1.4 wt % H_2O, with the balance being 98.6 wt % of argon after flame sealing, as determined by the equilibrium partial pressure of H_2O at 25 °C, with detailed calculations provided in the Supporting Information. Future studies can control this moisture level by controlling the sample preparation temperature. For the sample−air, it was directly transferred out of glovebox for flame sealing, and thus the air was sealed in the quartz capillary, which was 4 wt % of H_2O and 23 wt % O_2. All the capillary samples were flame-sealed using a miniature benchtop hydrogen torch (Rio grade). The concentration of impurities was calculated based on the equilibrium conditions of moisture and regular air in the atmosphere.

For the in situ corrosion experiments, each sealed double-capillary sample was heated to 500 °C with a 50 °C min^{-1} ramping rate and held isothermal for 2.5 h at the FXI beamline. The X-ray incident energy was 8.4 keV, just above the Ni K-edge (8.333 keV), thus could provide a sufficient transmission signal and good contrast for the Ni−20Cr wire. The field of view was 55.3 × 46.7 μm^2 with an effective pixel size of 43.2 nm by camera binning of 2 × 2. For each tomography scan, an exposure time of 0.05 s was used to capture ∼900 projections in a fly scan mode, with a total acquisition time of 1.5−2 min per scan. 2D XANES imaging was conducted across the Ni K-edge with the exposure time of 0.05 s at the end of the isothermal heating before cooling down the sample.

The tomography data were reconstructed using the "gridrec" method implemented in Tomopy.[39] The tomographic reconstruction stack images were cropped using the Crop3D plugin in ImageJ freeware[40] and then aligned using automatic registration operator based on the ITKElastix project[41] in Tomviz (version 1.10), an open-source software package.[42] The aligned images were segmented with the Trainable Weka Segmentation method in ImageJ. The "segment anything model",[43] was applied to separate the microwire region without precipitates. Finally, the processed stack images were virtualized in a 3D view using Dragonfly software version 2020.1 (Comet Technologies Canada Inc.).[44] Selected microwires and precipitates visualized in 3D were isolated for the volume and surface area calculations using Dragonfly software. The XANES imaging data and the extracted spectra were processed using PyXAS[29] and Athena software.[45] A corrosion depth calculation method[22] was used to understand the grain boundary corrosion, which is listed in details in Figure S1.

2.3. STEM Sample Preparation and Characterization.

The inner capillary containing the Ni−20Cr microwire after in situ synchrotron TXM was carefully taken out and placed in a membrane box in a glovebox. The membrane boxes were sealed in an aluminized Mylar bag under argon and then shipped to the Idaho National Laboratory (INL) for further scanning transmission electron spectroscopy analysis. The inner capillaries containing the Ni−20Cr wires were carefully broken by crushing it with an SEM stub with copper tape inside the inert atmosphere glovebox. The corroded Ni−20Cr wires along with surface salt were removed by using fine tweezers and placed on an SEM stub with carbon tape. The samples were vacuum sealed inside the glovebox and transferred to a scanning electron microscope equipped with a focused ion beam (FEI Quanta FEG dual beam) for TEM lamellae preparation using in situ lift out technique at the Center for Advanced Energy Studies (CAES) at Idaho National Laboratory (INL). TEM lamellae were loaded into a vacuum transfer holder inside a small inert atmosphere glovebox (Cleatech, LLC.) to mitigate exposure to air. The lamellae were analyzed using a Thermo Scientific Titan Themis 200 TEM equipped with SuperX energy dispersive X-ray spectroscopy and a Gatan Continuum ER EELS system at the Irradiated Materials Characterization Laboratory (IMCL) at INL.

3. RESULTS AND DISCUSSION

3.1. In-Situ 3D Morphological Evolution of Sample Sealed under Vacuum in LiCl−KCl at 500 °C.

To gain a better understanding of the effect of vacuum conditions and purified salt on the corrosion of Ni−20Cr in molten LiCl−KCl, the 2D *XY* and *XZ* pseudocross-sectional views and 3D volume rendering of the sample−vacuum at different reaction times in molten LiCl−KCl salt at 500 °C are shown in Figure S2 and Video S1 .

As seen in the *XY* view, there are three features with different X-ray attenuations in the image, as indicated by arrows with different colors: Ni−20Cr microwire (blue), molten salt (red), and empty region (yellow), from high to low X-ray attenuation. Sample−vacuum at room temperature (RT) is considered the pristine state, and the morphologies of sample−moisture and sample−air at room temperature are similar to that of sample−vacuum. The pristine state of a microwire has also been characterized by using STEM in our previous study.[26] The sample−vacuum was immersed in the molten salt, and there was no visible corrosion phenomenon at the metal−salt interface, such as the formation of a porous structure and grain boundary attack. Compared with the sample−vacuum at initial state, the microwire sample remains in a cylindrical shape without measurable morphological change even after ∼2 h at 500 °C. The results show that the impurity level was well controlled to be at a minimum level in the sample−vacuum system through the purification processes. In addition, it was experimentally confirmed that pure molten LiCl−KCl salt was not able to react with Ni or Cr in the Ni−20Cr alloy.

3.2. In-Situ 3D Morphological Evolution of Sample Sealed with Moisture in LiCl−KCl at 500°C.

Since there was no significant corrosion of the sample under vacuum conditions, the effect of moisture on corrosion in molten salt was then investigated by introducing approximately 1.4 wt % of H_2O in Ar. The 2D *XY* and *XZ* pseudocross-sectional views, 3D morphological changes, specific surface area, and corrosion depth of sample−moisture at different reaction times in molten

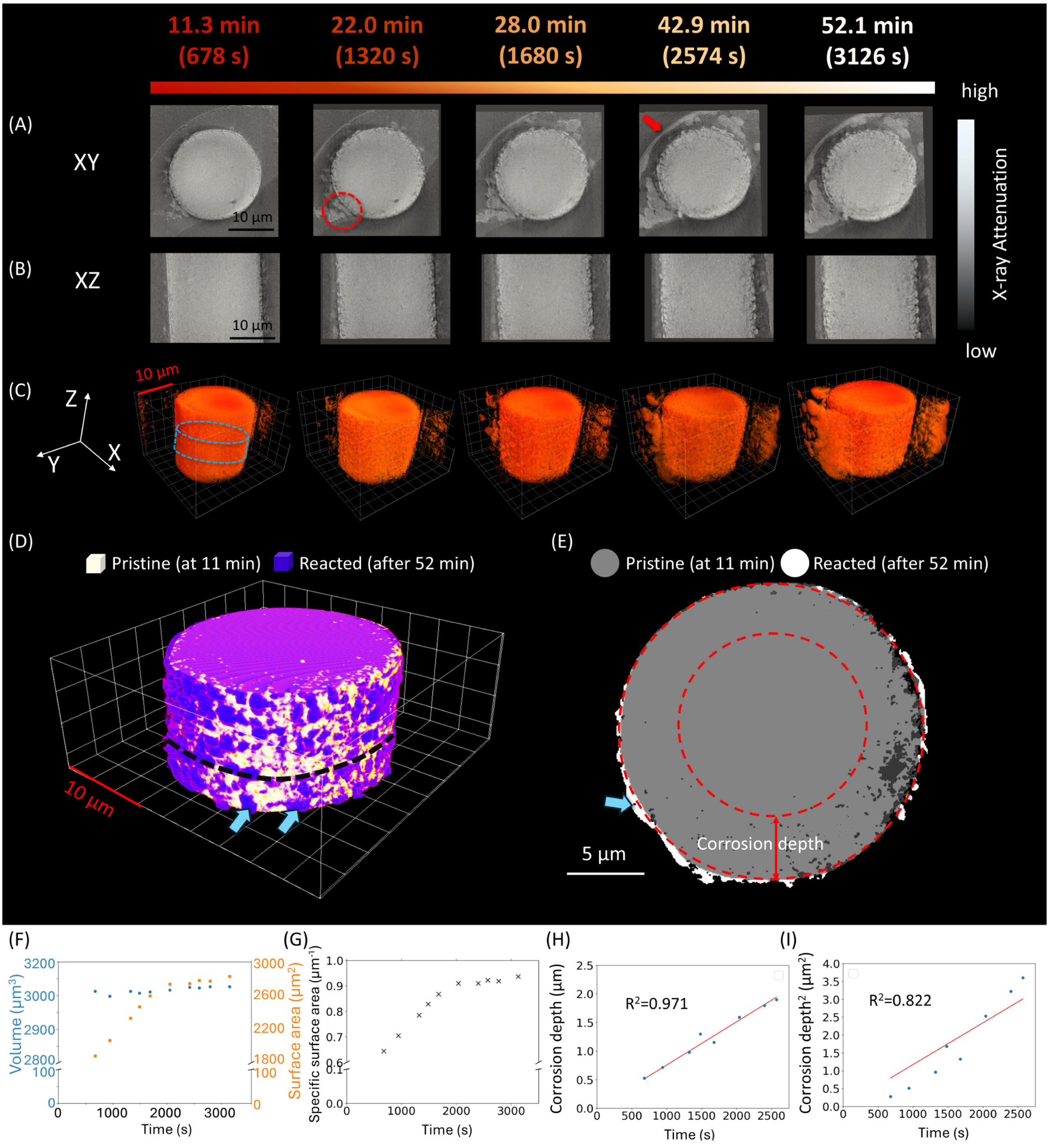

Figure 2. 3D morphological evolution, specific surface area, and corrosion depth of Ni−20Cr microwire in LiCl−KCl with 1.4 wt % H_2O in argon gas at 500 °C as a function of reaction time: (A,B) *XY* and *XZ* pseudocross-sectional views with region highlighted with a red circle indicating precipitate formed during the corrosion. (C) 3D volume rendering. (D) 3D visualization of the microwire in its pristine state (at 11 min) overlapped with the one reacted after 52 min, based on cropped images for the region highlighted with the blue-dash cylinder in (C). (E) Cross-sectional (*XY*) view of the microwire cylinder, corresponding to the slice highlighted by the black dashed curve in (D). 3D morphological quantifications of the Ni−20Cr microwire: (F) volume and surface area changes of the wire. (G) Specific surface area (surface area divided by volume) change. Plot of (H) corrosion depth vs time and (I) square of corrosion depth vs time with a linear fitting intercepting the origin point (0,0) and the goodness of fit.

LiCl−KCl salt at 500 °C are shown in Figure 2 and additional morphological evolution is shown in Video S2.

As shown in Figure 2(A−C), grain boundary attack was observed at the metal−salt interface in ~ 11 min and became more severe with increased time. The corrosion was likely due to the dissolution of Cr, as the redox potentials of Cr^{2+}/Cr and Cr^{3+}/Cr are lower than Ni^{2+}/Ni in molten chloride salt.[3] When Cr atoms at the grain boundary dissolved, Ni atoms merged

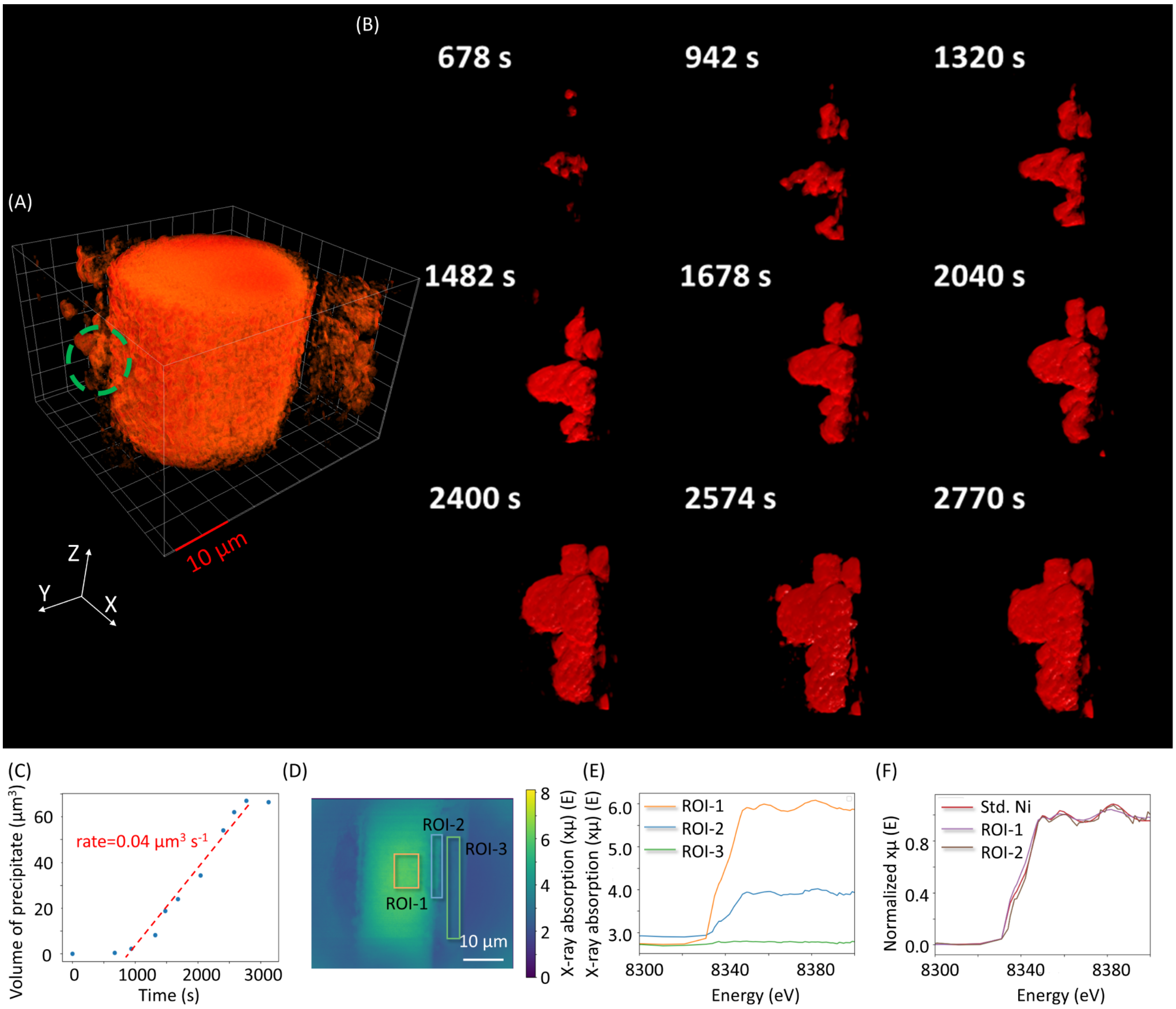

Figure 3. Morphological evolution of precipitate formed during the corrosion and 2D XANES images of sample−moisture in LiCl−KCl: (A) a representative 3D volume rendering of Ni−20Cr with a highlighted region of the precipitate cluster. (B) Zoom-in view of the morphological evolution of a cluster of precipitate in the region highlighted by a green circle in (A). (C) Plot showing that volume of precipitate increased with time, at a constant rate of 0.04 $\mu m^3\ s^{-1}$ during 1320−2770 s reaction time. (D) Representative frame from the 2D XANES spectroscopic imaging with three ROIs on the sample, at interface, and in the salt. (E) Ni K-edge XANES spectra at three ROIs without normalization. (F) Normalized XANES spectra of ROI-1 and ROI-2 compared with Ni standard spectrum. The measurement was conducted on the sample at 500 °C.

onto those vacancies forming a Ni-enriched layer that passivated further grain surface corrosion.[34] Consequently, the corrosion penetrated along the grain boundaries rather than broadening laterally. The precipitate observed in the salt, with some attached to the inner capillary wall (red arrow), might be Cr_2O_3, which will be further discussed in the next section and in the TEM sample analysis.

To quantify the morphological changes behavior of the Ni−20Cr wire, the precipitates were excluded from the 3D images using the "segment anything model".[43] Further quantification was then performed in the blue-dashed cylindrical region, as shown in Figure 2C, after segmentation and cropping. Figure 2D shows the microwire in its pristine state (at 11 min) overlaid with the microwire after 52 min of reaction. And one of the cross-sectional (*XY*) views of the microwire cylinder is shown in Figure 2E, corresponding to the slice highlighted by the black dashed curve. The blue arrows indicate that the diameter of the microwire after 52 min of reaction is larger than in its pristine state. This may suggest the formation of corrosion products on the surface during the reaction. To investigate the corrosion mechanisms along the grain boundaries, the corrosion depth was calculated, with an example highlighted by the red arrow in Figure 2E. Figure S1 illustrates the detailed calculation method based on the *XY* pseudo cross-sectional images in the blue-dashed cylindrical region over time. The volume, surface area, specific surface area (surface area divided by volume), and corrosion depth were calculated based on the segmented 3D X-ray tomography data, as shown in Figure 2F−I. In Figure 2F, the unchanged volume coupled with a rapid increase in surface area up to 2000 s of elapsed time indicated that intergranular corrosion occurred in the sample. The constant volume over time might be due to oxides forming at the interface, despite the dissolution of some Cr. This also can be evidenced by the increased diameter of the microwire, as shown in Figure 2D,E. After 2000 s, the surface area and specific surface area, as shown in Figure 2G, increased at a slower rate, indicating a reduced corrosion rate and a faster coarsening process. The

https://doi.org/10.1021/acsami.4c23034
ACS Appl. Mater. Interfaces 2025, 17, 28764−28776

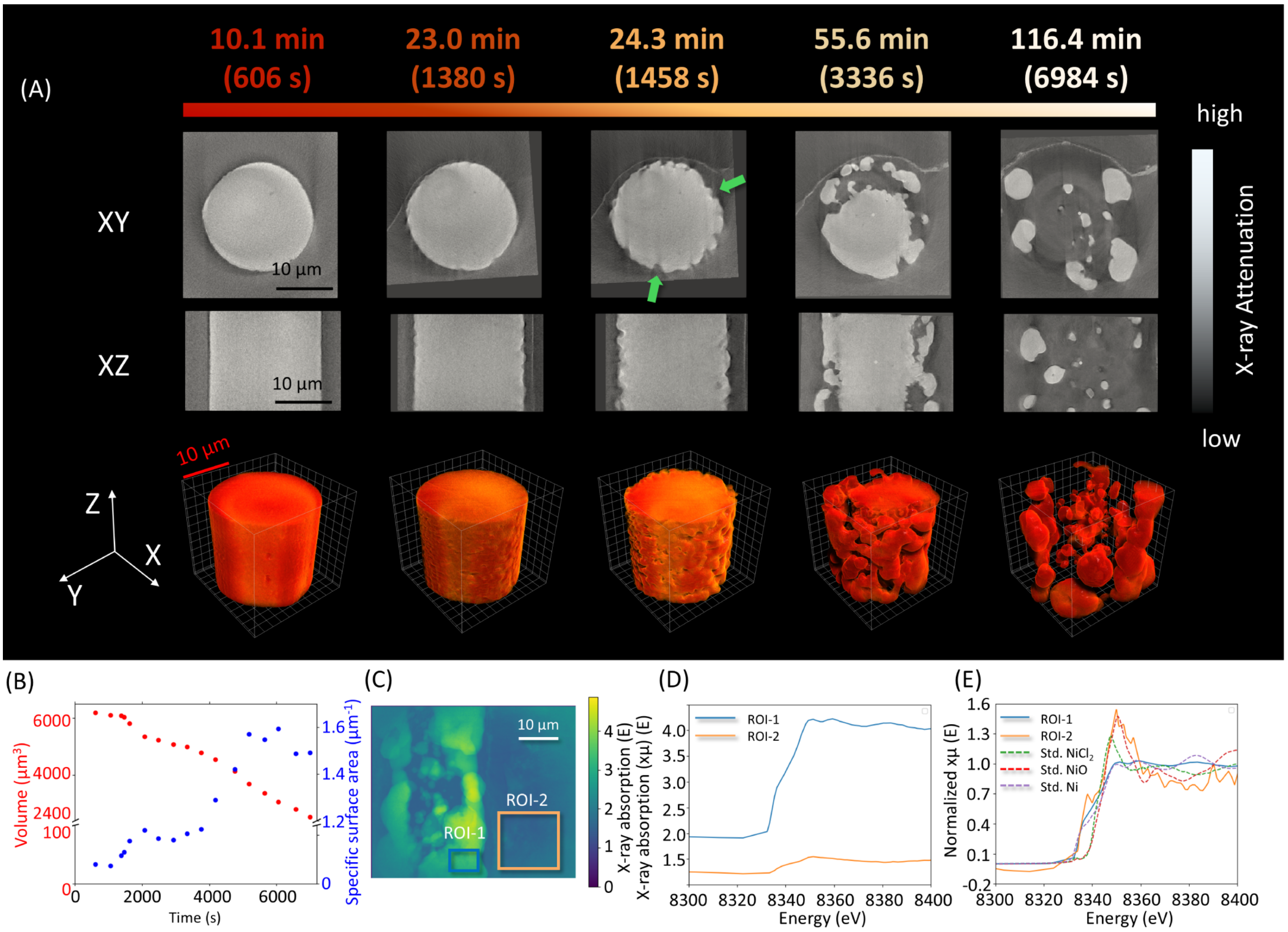

Figure 4. Morphological evolution and 2D XANES images of sample−air in LiCl-KCl at 500 °C as a function of reaction time: (A) *XY*, *XZ* pseudocross-sectional views and 3D volume rendering. (B) specific surface area of the sample−air as a function of reaction time. (C) Representative frame from the 2D XANES spectroscopic imaging with two ROIs on the sample, and in the salt with their Ni K-edge XANES spectra; (D) Ni K-edge XANES spectra at two ROIs; (E) normalized XANES spectrum of ROI-1 and ROI-2 compared with Ni, NiO, and $NiCl_2$ standard spectra.

slower corrosion rate was due to the depletion of oxidants in the salt, while the faster coarsening process resulted from the small features generated during corrosion. The "small features" refer to the voids and corroded metal structures with concave and convex curvatures that form at the interface during the corrosion process, which evolve to larger features during the coarsening process as shown in Figure S3. The plots of corrosion depth vs time and square of corrosion depth vs time are shown in Figure 2(H−I). As the corrosion depth is 0 when time is equal to 0, the power law fitting was constrained to intercept at the origin. A linear relationship between the time and corrosion depth with higher goodness of fit (R^2 = 0.971) shown in Figure 2H indicates that the corrosion is limited by an interfacial controlled process rather than long-range-controlled diffusion.[22] The plot of corrosion depth vs time with standard deviation is shown in Figure S4. Therefore, the long-range controlled diffusion, including the inward diffusion of impurity oxidants and (or) the outward diffusion of corrosion-produced ions (Cr ions), through the pores occurred more rapidly. In contrast, the reaction between oxidants and Cr, and (or) the diffusion of Ni along the metal-salt interface (both are interfacial controlled processes), were the rate-limited process. After approximately 3000 s, the sample−moisture exhibited minimal morphological changes, suggesting that the corrosion and coarsening process had reached a relatively stable state.

To further understand the formation of corrosion products in the salt, a region within the insoluble precipitates was isolated to investigate its formation and growth kinetics. Figure 3 shows the morphology and volume quantification of the isolated insoluble precipitate as well as 2D XANES imaging of the entire wire along with XANES spectra from selected regions.

The morphological evolution of the precipitates in the highlighted region in Figure 3A is shown in Figure 3B. Their volume increased at a constant rate of 0.04 $\mu m^3\ s^{-1}$ from 1320 to 2770 s, indicating a steady reaction rate between ions forming the insoluble precipitates (Figure 3C). The precipitate product might be NiO or Cr_2O_3, as metal oxides have low solubility in molten chloride salt.[46] To determine the chemical compositions in the salt and near the interface between microwire and salt, 2D XANES imaging at the Ni K-edge was conducted at three locations for the sample reacted for ~60 min as shown in Figure 3D. Region of interest (ROI)-1 was the region of microwire, ROI-2 was near the interface, and ROI-3 was the region in the salt. In Figure 3E, the XANES spectrum

https://doi.org/10.1021/acsami.4c23034

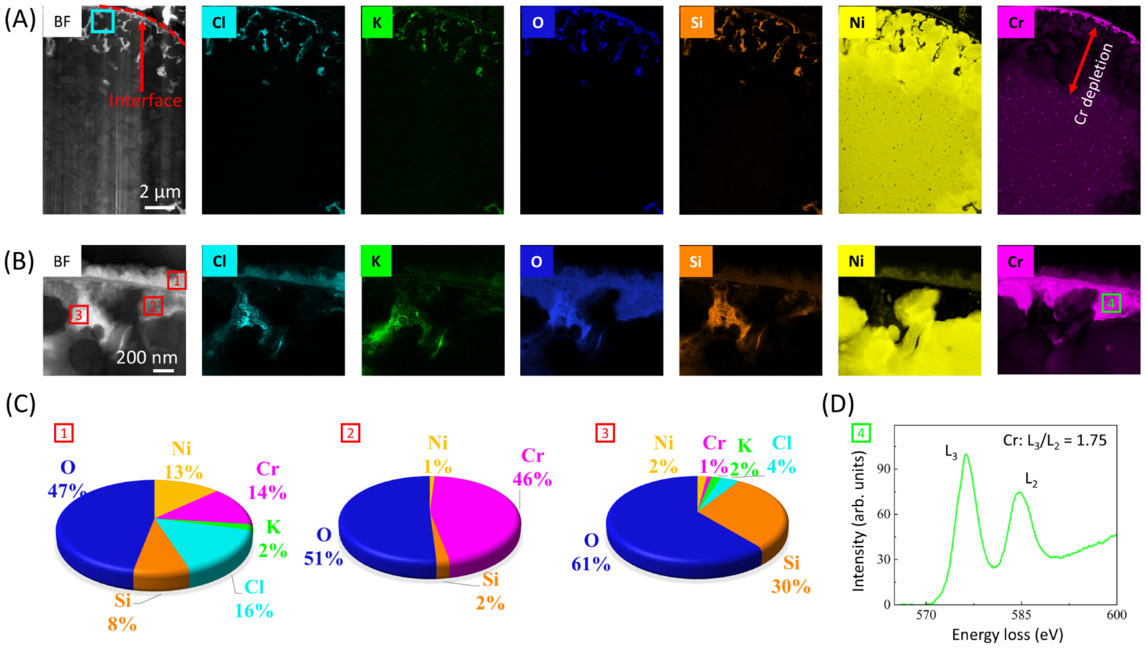

Figure 5. STEM-EDS-EELS analysis of a sample−moisture after corrosion in LiCl−KCl molten salt: (A,B) STEM bright-field image of the interface region of salt and alloy and its corresponding EDS mapping, (A) the whole region, and (B) the blue rectangle region as shown in (A). (C) EDS elemental distributions in region 1, region 2, and region 3, and (D) EELS analysis of upper Cr−O layer at region 4 (same location as region 2).

of ROI-3 from the region of salt including the precipitates shows a negligible amount of Ni. Thus, the precipitate is likely a Cr_2O_3 species, and the actual formation will be further discussed in the TEM characterization. Furthermore, as shown in Figure 3F, the uncorroded regions within the wire and near the interface remained as metallic Ni, as the normalized XANES spectra of ROI-1 and ROI-2 were consistent with those of the metallic Ni standard reference.

3.3. In-Situ 3D Morphological Evolution of Sample−Air in LiCl−KCl at 500°C.

To understand the effect of air on corrosion, the corrosion of Ni−20Cr in a sealed air atmosphere within the molten LiCl-KCl salt was studied at the FXI beamline. The 2D *XY* and *XZ* pseudocross-sectional views and 3D morphological changes of sample−air at different reaction times in molten LiCl-KCl salt at 500 °C are shown in Figure 4A and Video S3.

The surface of the sample roughened rapidly after ∼23 min, displaying concave and convex features. The initial lack of observed morphological change might be because it took time for the impurity to react with or dissolve into the salt. Within 2 min from that, the surface morphology changed significantly, with surface voids formed and increased surface roughness (green arrows). Unlike grain boundary corrosion, Ni lost its passivation effect with the presence of both O_2 and H_2O impurities. Ni atoms did not merge to the adjacent grain surface but instead dissolved into the salt. This is evidenced by the Ni signal detected in the salt, as shown in the XANES image (Figure 4C,D) and TEM/EDS results, which will be discussed further. Thus, the grain boundaries continued to broaden over time but the corrosion did not penetrate significantly deeper into the material. With continued corrosion in the molten salt, the microwire degraded significantly, with uniform corrosion attacking at the interfaces with relatively consistent dissolution of Ni and Cr. A similar severe degradation was observed on the surface of some bulk Ni-based alloys in a molten salt environment with air cover.[47] Eventually, the sample−air broke apart into small pieces after 116 min without precipitate forming in the molten salt in the presence of O_2. The absence of precipitate might be due to the formation of soluble corrosion products, which will be further discussed in the TEM sample analysis.

The volume and specific surface area were calculated and are plotted in Figure 4B. The volume decreased gradually until the end of the experiment due to corrosion. For the specific surface area, it increased rapidly in the early stage but then decreased between 2000 and 3000 s. The specific surface area increase might be due to the dissolution of elements, which generated large amounts of free surfaces. While the decrease in specific surface area might be attributed two to possible mechanisms: 1) smaller features merged into larger and more stable structures to minimize the total surface energy.[48] 2) Another possibility was that smaller features were completely dissolved in the molten salt. Following the initial rapid increase in the specific surface area, after ∼3000 s, a complex simultaneous dissolution and coarsening occurred, resulting in a gradual increase in the specific surface area. After ∼5000 s, the specific surface area remained stable while the volume continued to decrease, possibly due to the homogeneous surface corrosion on the fragmented features.

The 2D XANES image of sample−air at the Ni K-edge after reaction in the molten LiCl-KCl salt at 500 °C is shown in Figure 4C, and the corresponding XANES spectra of different ROIs on the sample and in the salt are shown in Figure 4D,E. The normalized XANES spectrum of ROI-1 on the sample was consistent with that of the metallic Ni standard. Additionally, the small edge jump at the Ni K-edge in the XANES spectrum of ROI-2 indicated a low concentration of Ni in the salt region, but it was not negligible. The normalized spectrum of ROI-2 in the salt region as shown in Figure 4(might be a mixture of NiO and metallic Ni. NiO observed in the molten chloride salt

https://doi.org/10.1021/acsami.4c23034
ACS Appl. Mater. Interfaces 2025, 17, 28764−28776

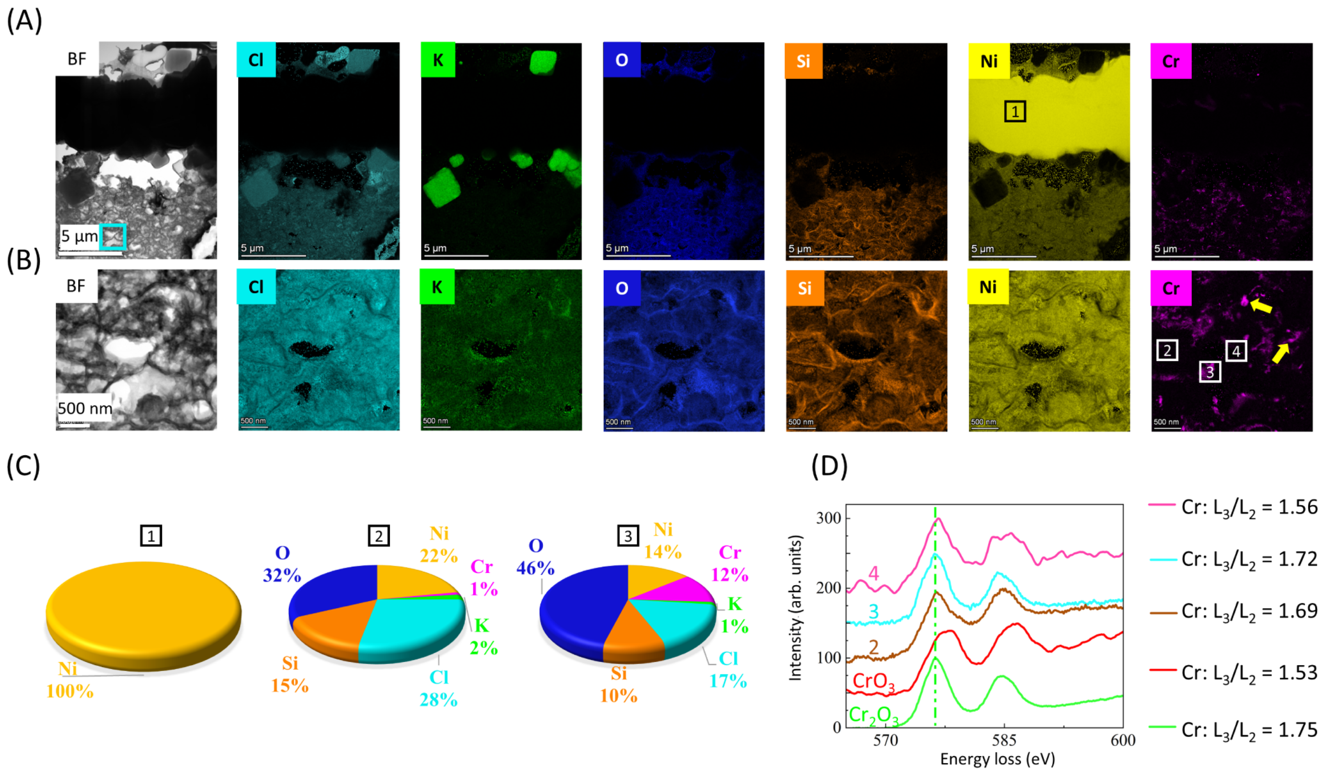

Figure 6. STEM−EDS−EELS analysis of a sample−air after corrosion in LiCl−KCl molten salt, showing the (A) STEM bright-field image of interface region of salt and alloy and its corresponding EDS mapping of the whole region, (B) STEM bright-field image of the blue rectangle region as shown in (A) and its corresponding EDS mapping, (C) EDS elemental distributions in region 1, region 2, and region 3, and (D) EELS analysis of region 2, region 3, region 4, and CrO$_3$ as well as Cr$_2$O$_3$ standard reference.

as a corrosion product from Ni−20Cr wire is consistent with our prior work.[49] The metallic Ni observed in the salt might be small fragmented parts or nanosized metallic debris detached from the sample.[50] Given the significant corrosion of the sample and the absence of precipitate, it is likely that both Ni and Cr dissolved into soluble corrosion products as ionic states in the salt. The dissolved Cr species will be further discussed in the TEM sample analysis. Consequently, sample−air fragmented into smaller components after approximately 116 min.

3.4. STEM/EDS/EELS Characterization on Sample−Moisture and Sample−Air Post Corrosion.

After synchrotron X-ray nanotomography, the same samples, including sample−moisture and sample−air, were characterized by STEM/EDS/EELS to investigate the elemental distributions and chemical states at the near-interface region. STEM images of sample−moisture after in situ TXM experiment, along with EDS and EELS analysis, are shown in Figure 5.

As shown in Figure 5A, grain boundary attack corrosion was observed on the sample with salt penetrating through the grain boundaries to the inner sample (Cl and K EDS mapping images). This finding is consistent with the morphology observed by in situ synchrotron X-ray nanotomography.[13,34] After corrosion, a Cr-depleted region was observed at the corrosion site, which was enriched with Ni. Figure 5B shows an enlarged view of the Cr-depleted region in Figure 5A, as indicated with a blue square. A Cr$_2$O$_3$ layer was found on the surface of the sample, and its elemental composition and oxidation state were confirmed as shown in Figure 5C,D, respectively. In Figure 5C, the composition of the layer in region 2 is enriched with Cr and O. In Figure 5D, the integrated intensity ratio of Cr L$_3$ and L$_2$ peaks in region 2 is 1.75, which matches the reference Cr$_2$O$_3$ (L$_3$/L$_2$ = 1.75) more closely than Cr (1.45) or Cr^{2+} (2.01) as listed in Table S1. Therefore, the presence of Cr on the outer surface layer and salt was in the form of Cr$_2$O$_3$. Unlike solid/gas interfacial corrosion, Cr$_2$O$_3$ was not directly produced from Cr metal and O$_2$ gas but from Cr^{3+} and the O^{2-} ion in molten salt. Because of a higher free energy at grain boundary region and the presence of Ni-enriched region at outer surface, a galvanic corrosion might take place at these two regions. Below the mechanism is proposed:

First, H$_2$O dissolves in the LiCl−KCl molten salt at elevated temperatures.[51] The dissolved H$_2$O reacts with LiCl as listed in reaction (1).[52−54] Although reaction (1) is not energetically favorable (Gibbs energy is positive) under standard conditions, this hydrolysis reaction can proceed with the continuous dissolution of the products, which consumed H$^+$.[52−54] The dissolved Li$_2$O is in an ionic state[55] as listed in the reaction (2). Indeed, all species involved in the reactions are in their ionic states in the molten salt. Thus, combining reactions (1) and (2) simply yields the ionization reaction of H$_2$O, as shown in reaction (3). Then, galvanic corrosion occurs between the grain boundary and the outer surface region. At the grain boundary, Cr dissolves as Cr^{3+} ions, releasing electrons according to reaction (4). Cr^{2+} ions are not considered in the reactions, as the final oxidation state of Cr in the salt is 3+. These electrons transfer to the Ni-enriched region, which presents a large area on the outer surface. Then, Cr^{3+} diffuses to the outer surface due to the concentration gradient. This long-range diffusion is faster than the interfacial diffusion process, which does not hinder further dissolution of Cr. In the Ni-enriched region, H$^+$ gains the electrons, forming H$_2$ gas, as

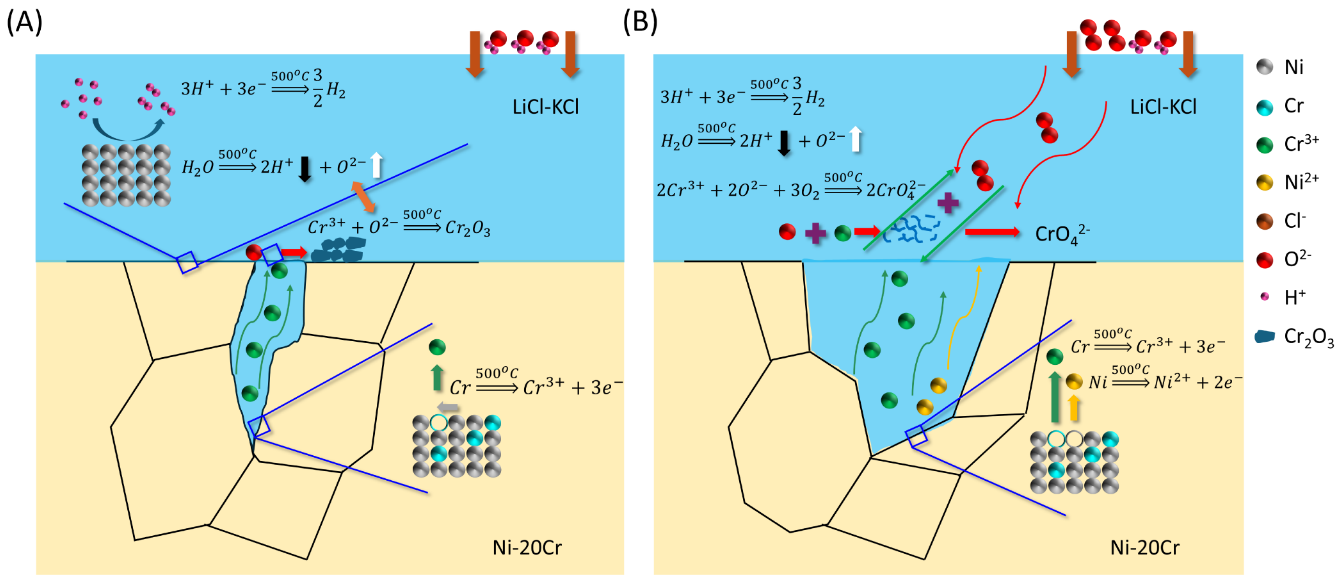

Figure 7. Schematic illustration of the reaction and diffusion mechanisms involved in the corrosion process of Ni−20Cr in molten LiCl−KCl at 500 °C with (A) sealed 1.4 wt % water in argon and (B) sealed air.

shown in reaction (5). As H^+ reacts in this Ni-enriched region, more O^{2-} is generated based on reaction (3). Consequently, Cr^{3+} reacts with O^{2-} at the outer surface and in salt regions with a higher concentration of O^{2-}, forming Cr_2O_3, as indicated in reaction (6).

$$\text{Salt region: } H_2O + 2LiCl \xrightarrow{500°C,\text{ in LiCl−KCl}} Li_2O + 2HCl \tag{1}$$

$$\text{Salt region: } Li_2O \xLeftrightarrow{500°C,\text{ in LiCl−KCl}} 2Li^+ + O^{2-} \tag{2}$$

$$\text{Combining (1) and (2): } H_2O \xLeftrightarrow{500°C,\text{ in LiCl−KCl}} 2H^+ + O^{2-} \tag{3}$$

$$\text{Grainboundary: } Cr \xRightarrow{500°C,\text{ in LiCl−KCl}} Cr^{3+} + 3e^- \tag{4}$$

$$\text{Ni − enriched region: } 3H^+ + 3e^- \xRightarrow{500°C,\text{ in LiCl−KCl}} \frac{3}{2}H_2(g) \tag{5}$$

$$\text{Ni − enriched and salt regions: } 3O^{2-} + 2Cr^{3+} \xRightarrow{500°C,\text{ in LiCl−KCl}} Cr_2O_3 \tag{6}$$

This Cr_2O_3 layer formed on the surface and explained and confirmed why the diameter of the wire increased during corrosion as discussed in Figure 2. The nucleation occurred in the salt region, and further growth of Cr_2O_3 was on the precipitates instead of directly forming at the interface. This observation partly explains why the literature reports that nonprotective and discontinuous Cr_2O_3 formed on Fe-based and Ni-based alloy samples, including austenitic stainless steel,[56] 304 stainless steel,[57] and superalloy *N*-2,[58] during corrosion in molten chloride salts. Some Si was observed in the salt region, which might be from the dissolution of the quartz capillary container. SiO_2 is stable in molten salt with a relatively low solubility of ∼1 ppm in NaCl−KCl−Na_2SO_4−K_2SO_4 eutectic molten salt with 10^{-5} mol/L O^{2-} at 550 °C.[46] However, SiO_2 might react with Li_2O (reactions 1−2) and form as several kinds of lithium silicate ($Li_xSi_yO_z$).[59] These lithium silicates might be dissolved into the molten salt and then observed by EDS mapping the salt region.

Here, two different corrosion mechanisms for the samples with moisture and with sealed air in LiCl−KCl molten salt are proposed, based on the 3D morphological changes discussed in previous sections. To further understand these differences, particularly regarding the formation and absence of oxide precipitates, STEM images of sample−air after the in situ TXM experiment, along with EDS and EELS analyses, are shown in Figure 6.

As shown in Figure 6A, a fragmented component of the wire was left in the salt, which was consistent with the 3D morphology observed in TXM experiments at the final stage. This fragmented component was pure Ni without Cr in it, as illustrated in the EDS mapping and confirmed with the EDS quantitative analysis in Figure 6C. Ni was not stable in LiCl−KCl molten salt with the presence of air, as a large amount of Ni was observed in the salt region. The homogeneous distribution of Ni in the salt region further confirmed that Ni was dissolved in the salt, which is illustrated in a prior section of XANES analysis in Figure 4. As shown in the Cr EDS mapping in Figure 6B, the distribution of Cr in the salt was not as homogeneous as that of Ni. It seemed that there were Cr compound precipitates (indicated with yellow arrow) formed during sample cooling down with small particle sizes as these precipitates were not observed in the TXM experiment at 500 °C. The elemental composition of the precipitate shown in the EDS analysis contained Cr, Cl, and O, indicating the precipitates might be chromium chloride and oxide. As the solubility of $CrCl_3$ increases with elevated temperatures (∼5 mol % at 500 °C and ∼10 mol % at 800 °C),[34] the observed $CrCl_3$ precipitates might be due to its lower solubility at room temperature in the salt. Cr_2O_3 precipitates are discussed in the following EELS analysis. Similar to the sample with moisture, Si was also observed in the salt in the EDS mapping shown in Figure 6A,B.

Further EELS analysis indicated that Cr^{6+} formed in the salt region (region 4) as shown in Figure 6(D). The mixed oxidation states of Cr^{3+} and Cr^{6+} were observed in regions 2 and 3. Cr_2O_3 initially formed following reactions (1−6) with water impurity only. However, in the presence of both O_2 and H_2O in molten LiCl−KCl salt, the concentration of O_2 and O^{2-} was higher in the system. The produced Cr_2O_3 might undergo further reaction (7) and generate Cr^{6+} species[60] in the salt.

$$2Cr_2O_3 + 3O_2 + 4O^{2-} \overset{500°C}{\Longleftrightarrow} 4CrO_4^{2-} \quad (7)$$

The solubility of Cr_2O_3 in molten chloride salt increases with higher concentrations of O^{2-} ions due to the formation of Cr^{6+} species.[60] Since a small amount of Cr_2O_3 precipitates was still observed in the salt (Figure 6B), not all Cr_2O_3 species converted to Cr^{6+} species. This reaction (reaction (7)) is likely fast, and the remaining Cr_2O_3 existed in small amounts and with a small particle size (~60 nm), which explains why no precipitates were observed in the salt during the corrosion of sample−air in molten LiCl−KCl salt at 500 °C in the TXM experiment. A recent study found the formation of K_2CrO_4 and Na_2CrO_4 rather than Cr_2O_3 in molten NaCl−KCl salt, after the corrosion of Fe−35Cr at 700 °C.[61] In addition, Li_2O can react with Cr_2O_3 to form chromate ions, which are soluble in molten LiCl-based salt.[62] In carbonate molten salt, a higher concentration of O^{2-} can also lead to the continuous dissolution of the Cr_2O_3 layer into soluble chromate.[63]

3.5. Influences of Impurity on Molten Salt Corrosion.

In this work, the corrosion of Ni−20Cr in a molten LiCl−KCl salt at 500 °C was observed to be an impurity-dependent process. In the absence of impurities under vacuum conditions, no significant morphological changes were detected in the sample. Severe grain boundary corrosion on the sample and a large quantity of precipitates in the salt were observed during corrosion in the presence of 1.4 wt % H_2O in argon. For the sample filled with sealed air, the sample eventually broke apart into small pieces with no precipitate observed at 500 °C.

To summarize the different corrosion mechanisms associated with various impurities, a schematic illustration is shown in Figure 7.

For the sample−moisture as illustrated in Figure 7A, water first dissolves into the salt, generating O^{2-} and H^+. H^+, acting as an oxidizing agent, initiates galvanic corrosion near the grain boundary: Cr dissolves as Cr^{3+} at the grain boundary (anodic reaction), while H^+ absorbs electrons in the Ni-enriched region, forming H_2 as the cathodic reaction product. At the grain boundary, Ni atoms merge with the adjacent grain surface as Cr dissolves, forming a passivation layer. Consequently, corrosion progresses along the grain boundary rather than widening it. In the Ni-enriched region, H_2O further takes part in the ionization reaction as H^+ is consumed, leading to a higher concentration of O^{2-}. Cr^{3+} generated at the grain boundary diffuses to the surface due to the concentration gradient, where it reacts with O^{2-} to produce a Cr_2O_3 precipitate.

For the sample−air reaction, as illustrated in Figure 7B, the cathodic reaction also produces H_2, leading to an increased concentration of O^{2-}. However, Cr_2O_3 formed by the reaction of Cr^{3+} and O^{2-} further reacts with O_2, producing a Cr^{6+} species. Since the Cr^{6+} species is soluble in molten salt, the precipitates were not observed during the experiment. Additionally, Ni participates in the anodic reaction, forming Ni^{2+} ions. This is supported by EDS mapping, which shows a homogeneous distribution of Ni species in the salt. Furthermore, 2D XANES mapping indicates that the Ni species in the salt region is NiO, likely due to the involvement of O_2 in the reaction. Consequently, the grain boundary broadens due to uniform corrosion with consistent dissolution of both Ni and Cr.

4. CONCLUSIONS

In this study, the 3D morphological and chemical evolution of Ni−20Cr microwires in eutectic LiCl−KCl molten salt at 500 °C with different amounts of water and oxygen contents were investigated using in situ synchrotron TXM and STEM techniques. This revealed distinct corrosion behaviors depending on the sample environment and the amount of impurities. The sample sealed under a vacuum showed no significant morphological changes, indicating effective impurity control and resistance to corrosion in pure molten salt. In contrast, the sample sealed with moisture exhibited significant grain boundary attack with a constant penetration rate (linear relationship between corrosion depth and time). Precipitates were observed at the outer surface and the salt regions, increasing at a constant rate over time with the formation of Cr_2O_3, which was confirmed by the STEM analysis. In the sample sealed with air, rapid surface roughening was observed initially, followed by the uniform surface corrosion of both Cr and Ni. The sample was eventually fragmented into smaller pieces without precipitate formation, highlighting the synergistic impact of O_2 and H_2O presence in the salt.

The STEM/EDS/EELS characterization of postcorrosion samples sealed with moisture and with air provides detailed insights into the corrosion mechanisms in molten LiCl-KCl salt at 500 °C. Significant grain boundary corrosion was observed in the sample sealed with moisture, while a fragmented component was detected in the sample sealed with air, which was consistent with the TXM results. In the sample sealed with moisture, the grain boundary corrosion-attacked region was depleted of Cr but enriched with Ni. Additionally, the Cr_2O_3 layer observed on the outer surface confirmed the precipitate composition found in TXM data analysis. Based on the observation of Cr_2O_3 in salt and outer surface regions, a corrosion mechanism is proposed, involving ion diffusion and galvanic corrosion between the Ni-enriched region and grain boundary corrosion region. Cr^{3+} produced at the grain boundary region diffused to the outer surface and further formed as Cr_2O_3 with O^{2-} in the salt. For the sample sealed with air, the fragmented component was nearly pure Ni, as confirmed with EDS analysis. The absence of precipitate and the presence of Cr^{6+} in the salt, detected by EELS analysis, indicated that the Cr_2O_3 precipitate might be further oxidized to a soluble Cr^{6+} species in the presence of O_2. This study highlights the complexity of corrosion mechanisms with different amounts of H_2O and O_2 impurities in molten salt, which will be important for developing corrosion mitigation methods and improving material performance in numerous high-temperature molten salt applications including nuclear and solar power generation and beyond. Synchrotron X-ray nanotomography coupled with STEM postanalysis is shown to be valuable tools in revealing the morphological changes and elemental distributions. Future studies investigating the role of microstructures such as grain boundaries and dislocations to determine their effects on the corrosion will be valuable, using high-resolution SEM and TEM, or specialized X-ray techniques such as X-ray topography. Additionally, conducting studies at higher temperatures will provide valuable insights on the temperature-dependent reaction and diffusion kinetics, including the rates and mechanisms controlling the morphological changes and chemical reactions.

■ ASSOCIATED CONTENT

Data Availability Statement

The digital data for all figures, tables, charts, and any other media contained in this publication and its associated Supporting Information files will be made accessible on the Zenodo repository, under Digital Object Identifier (DOI): 10.5281/zenodo.14026603

SI Supporting Information

The Supporting Information is available free of charge at https://pubs.acs.org/doi/10.1021/acsami.4c23034.

> STEM EELS analysis, L_3/L_2 integrated intensity ratios of standard references; calculation method of corrosion depth for corrosion of Ni–20Cr microwires in LiCl–KCl molten salt at 500 °C; details to determine the 1.4 wt % of H_2O in Ar for sample–moisture; morphological evolution of sample–vacuum Ni–20Cr in LiCl–KCl at 500 °C as a function of heating time; coarsening of smaller features (voids and corroded metal structures) into larger features at the surface of sample–moisture Ni–20Cr in LiCl–KCl at 500 °C over time; plot of corrosion depth with standard deviation vs time with a linear fitting intercepting the origin point (0,0) and the goodness of fit for Ni–20Cr microwire corrosion in LiCl–KCl molten salt at 500 °C (PDF)
>
> Videos including: 1. The 3D morphology of Ni-20Cr corroded in eutectic LiCl–KCl (59.2–41.8 mol %) sealed under vacuum condition at 500 °C for 120 min (AVI)
>
> 2. The 3D morphology of Ni-20Cr corroded in eutectic LiCl-KCl (59.2–41.8 mol %) sealed with 1.4 wt % moisture and 98.6 wt % argon at 500 °C for 52 min (AVI)
>
> 3. The 3D morphology of Ni-20Cr corroded in eutectic LiCl-KCl (59.2–41.8 mol %) sealed with room air at 500 °C for 120 min (AVI)

■ AUTHOR INFORMATION

Corresponding Authors

Yuxiang Peng – *Department of Materials Science and Chemical Engineering, Stony Brook University, Stony Brook, New York 11790, United States;* orcid.org/0000-0002-8688-3654; Email: peng.yuxiang@stonybrook.edu

Yu-chen Karen Chen-Wiegart – *Department of Materials Science and Chemical Engineering, Stony Brook University, Stony Brook, New York 11790, United States; National Synchrotron Light Source II (NSLS-II), Brookhaven National Laboratory, Upton, New York 11793, United States;* orcid.org/0000-0003-4445-2159; Email: Karen.Chen-Wiegart@stonybrook.edu

Authors

Kaustubh K. Bawane – *Advanced Characterization Department, Idaho National Laboratory, Idaho Falls, Idaho 83415, United States*

Xiaoyang Liu – *Department of Materials Science and Chemical Engineering, Stony Brook University, Stony Brook, New York 11790, United States; Advanced Photon Source, Argonne National Laboratory, Lemont, Illinois 60439, United States;* orcid.org/0000-0002-9326-2135

Xiaoyin Zheng – *Department of Materials Science and Chemical Engineering, Stony Brook University, Stony Brook, New York 11790, United States*

Mingyuan Ge – *National Synchrotron Light Source II (NSLS-II), Brookhaven National Laboratory, Upton, New York 11793, United States;* orcid.org/0000-0001-5682-7443

Xianghui Xiao – *National Synchrotron Light Source II (NSLS-II), Brookhaven National Laboratory, Upton, New York 11793, United States*

Ellie M. Kim – *Department of Chemistry, University of Tennessee Knoxville, Knoxville, Tennessee 37996, United States*

Phillip W. Halstenberg – *Department of Chemistry, University of Tennessee Knoxville, Knoxville, Tennessee 37996, United States;* orcid.org/0000-0002-6030-4503

Sheng Dai – *Department of Chemistry, University of Tennessee Knoxville, Knoxville, Tennessee 37996, United States; Chemical Sciences Division, Oak Ridge National Laboratory, Oak Ridge, Tennessee 37831, United States;* orcid.org/0000-0002-8046-3931

James F. Wishart – *Chemistry Division, Brookhaven National Laboratory, Upton, New York 11973, United States;* orcid.org/0000-0002-0488-7636

Complete contact information is available at: https://pubs.acs.org/10.1021/acsami.4c23034

Author Contributions

Y.P.: conceptualization, investigation and analysis, writing – original draft, review and editing. K.K.B.: STEM/EDS/EELS analysis, review and editing. X.L.: investigation and analysis. X.Z.: TXM data analysis. M.G. and X.X.: synchrotron TXM investigation. E.M.K. and P.W.H.: salt purification. S.D.: salt purification, consultant. J.F.W.: conceptualization, supervision, writing – review and editing. Y.K.C.-W.: conceptualization, investigation and analysis, supervision, writing – original draft, review and editing.

Funding

This work was supported as part of the Molten Salts in Extreme Environments (MSEE) Energy Frontier Research Center, funded by the U.S. Department of Energy (DOE), Office of Science, Basic Energy Sciences. BNL, ORNL, and INL are operated under DOE contracts DE-SC0012704, DE-AC05–00OR22725, and DE-AC07–051D14517, respectively. Work at Stony Brook University and the University of Tennessee Knoxville was supported by MSEE through a subcontract from BNL.

Notes

The authors declare no competing financial interest.

■ ACKNOWLEDGMENTS

This work was supported as part of the Molten Salts in Extreme Environments (MSEE) Energy Frontier Research Center, funded by the U.S. Department of Energy (DOE), Office of Science, Basic Energy Sciences. BNL, ORNL, and INL are operated under DOE contracts DE-SC0012704, DE-AC05-00OR22725, and DE-AC07-051D14517, respectively. Work at the University of Tennessee, Knoxville, and Stony Brook University was supported by MSEE through a subcontract from BNL. This research used resources and the 18-ID (Full Field X-ray Imaging, FXI) beamline of the National Synchrotron Light Source II, a U.S. DOE Office of Science User Facility operated for the DOE Office of Science by Brookhaven National Laboratory under Contract DE-SC0012704. The FIB and STEM facilities are as part of the Nuclear Science User Facilities. The authors also thank MSEE EFRC members, Dr. Adrien Couet and Dr. Katsuyo Thornton for their invaluable suggestions and comments during center meeting discussions.

REFERENCES

(1) Ding, W.; Bauer, T. Progress in research and development of molten chloride salt technology for next generation concentrated solar power plants. *Eng.* **2021**, *7*, 334−347.

(2) Fernández, A. G.; Cabeza, L. F. Corrosion evaluation of eutectic chloride molten salt for new generation of CSP plants. Part 2: Materials screening performance. *J. Energy Storage.* **2020**, *29*, 101381.

(3) Guo, S.; Zhang, J.; Wu, W.; Zhou, W. Corrosion in the molten fluoride and chloride salts and materials development for nuclear applications. *Prog. Mater. Sci.* **2018**, *97*, 448−487.

(4) Roper, R.; Harkema, M.; Sabharwall, P.; Riddle, C.; Chisholm, B.; Day, B.; Marotta, P. Molten salt for advanced energy applications: A review. *Ann. Nucl. Energy.* **2022**, *169*, 108924.

(5) Sridharan, K.; Anderson, M.; Allen, T.; Corradini, M. *Liquid salts as media for process heat transfer from VHTR's: forced convective channel flow thermal hydraulics, materials, and coating DOE/ID 14826*; University of Wisconsin-Madison: Madison, WI, 2012.

(6) Xu, X.; Wang, X.; Li, P.; Li, Y.; Hao, Q.; Xiao, B.; Elsentriecy, H.; Gervasio, D. Experimental Test of Properties of KCl−$MgCl_2$ Eutectic Molten Salt for Heat Transfer and Thermal Storage Fluid in Concentrated Solar Power Systems. *J. Sol. Energy Eng.* **2018**, *140* (5), 051011.

(7) Taube, M. *Fast reactors using molten chloride salts as fuel INFCE/DEP./WG−8/75.*; International Atomic Energy Agency (IAEA): Switzerland, 1978.

(8) Forsberg, C. W. Molten-salt-reactor technology gaps.In *Internationa l Congress on Advances in Nuclear Power Plants (ICAPP'06)*. Citeseer: USA Reno, NV, 2006, 4−8.

(9) LeBlanc, D. Molten salt reactors: A new beginning for an old idea. *Nucl. Eng. Des.* **2010**, *240*, 1644−1656.

(10) Sridharan, K.; Allen, T.; Anderson, M.; Simpson, M. *Thermal properties of LiCl-KCl molten salt for nuclear waste separationDOE/NEUP-09−780*; University of Wisconsin: Madison, WI, United States; Idaho National Lab., ID, United States, 2012.

(11) Ravi Shankar, A.; Mathiya, S.; Thyagarajan, K.; Kamachi Mudali, U. Corrosion and microstructure correlation in molten LiCl-KCl medium. *Metall. Mater. Trans. A* **2010**, *41*, 1815−1825.

(12) Rao, C. J.; Ningshen, S.; Mallika, C.; Mudali, U. K. Molten salt corrosion behavior of structural materials in LiCl-KCl-UCl_3 by thermogravimetric study. *J. Nucl. Mater.* **2018**, *501*, 189−199.

(13) Bawane, K.; Liu, X.; Gakhar, R.; Woods, M.; Ge, M.; Xiao, X.; Lee, W.-K.; Halstenberg, P.; Dai, S.; Mahurin, S.; et al. Visualizing time-dependent microstructural and chemical evolution during molten salt corrosion of Ni-20Cr model alloy using correlative quasi in situ TEM and in situ synchrotron X-ray nano-tomography. *Corros. Sci* **2022**, *195*, 109962.

(14) Villada, C.; Ding, W.; Bonk, A.; Bauer, T. Engineering molten $MgCl_2$−KCl−NaCl salt for high-temperature thermal energy storage: Review on salt properties and corrosion control strategies. *Sol. Energy Mater. Sol. Cells* **2021**, *232*, 111344.

(15) Ding, W.; Shi, H.; Xiu, Y.; Bonk, A.; Weisenburger, A.; Jianu, A.; Bauer, T. Hot corrosion behavior of commercial alloys in thermal energy storage material of molten $MgCl_2$/KCl/NaCl under inert atmosphere. *Sol. Energy Mater. Sol. Cells* **2018**, *184*, 22−30.

(16) Susskind, H.; Hill, F.; Green, L.; Kalish, S.; Kukacka, L.; McNulty, W.; Wirsing, E., Jr. *Corrosion studies for a fused salt-liquid metal extraction process for the liquid metal fuel reactor BNL-585*; Brookhaven National Lab: Upton, NY, 1960.

(17) Eliaz, N.; Shemesh, G.; Latanision, R. Hot corrosion in gas turbine components. *Eng. Fail. Anal.* **2002**, *9*, 31−43.

(18) Ghaznavi, T.; Persaud, S. Y.; Newman, R. C. Electrochemical corrosion studies in molten chloride salts. *J. Electrochem. Soc.* **2022**, *169*, 061502.

(19) Liu, X.; Quan, F.; Zeng, X.; Li, W.; Yuan, Y.; Wang, J.; Wang, Z.; Li, J.; He, F.; Wang, J. Corrosion behavior of dual-phase Fe36Ni36Al17Cr10Mo1 multi-principal component alloy in LiCl−KCl−CsCl molten salt at 700 °C. *J. Mater. Sci.* **2024**, *59* (46), 21433−21447.

(20) Raiman, S. S.; Lee, S. Aggregation and data analysis of corrosion studies in molten chloride and fluoride salts. *J. Nucl. Mater.* **2018**, *511*, 523−535.

(21) Liu, X.; Ronne, A.; Yu, L.-C.; Halstenberg, P.; Xiao, X.; Lee, W.-K.; Dai, S.; Ge, M.; Chen-Wiegart, Y.-C. K. Heterogeneous 3D Morphological Evolution of Ni Microparticles in Molten Salts: Visualized by Operando Synchrotron X-ray Nano-tomography. *JOM* **2023**, *75*, 1006−1018.

(22) Liu, X.; Ronne, A.; Yu, L.-C.; Liu, Y.; Ge, M.; Lin, C.-H.; Layne, B.; Halstenberg, P.; Maltsev, D. S.; Ivanov, A. S.; et al. Formation of three-dimensional bicontinuous structures via molten salt dealloying studied in real-time by in situ synchrotron X-ray nano-tomography. *Nat. Commun.* **2021**, *12* (1), 3441.

(23) Ding, W.; Gomez-Vidal, J.; Bonk, A.; Bauer, T. Molten chloride salts for next generation CSP plants: Electrolytical salt purification for reducing corrosive impurity level. *Sol. Energy Mater. Sol. Cells* **2019**, *199*, 8−15.

(24) Kamali, A. R.; Fray, D. J.; Schwandt, C. Thermokinetic characteristics of lithium chloride. *J. Therm. Anal. Calorim.* **2011**, *104*, 619−626.

(25) D'Souza, B.; Zhuo, W.; Yang, Q.; Leong, A.; Zhang, J. Impurity driven corrosion behavior of HAYNES® 230® alloy in molten chloride Salt. *Corros. Sci.* **2021**, *187*, 109483.

(26) Ronne, A.; He, L.; Dolzhnikov, D.; Xie, Y.; Ge, M.; Halstenberg, P.; Wang, Y.; Manard, B. T.; Xiao, X.; Lee, W.-K.; et al. Revealing 3D morphological and chemical evolution mechanisms of metals in molten salt by multimodal microscopy. *ACS Appl. Mater. Interfaces.* **2020**, *12* (15), 17321−17333.

(27) Wang, Y.; Gao, J.; Sun, W.; Shahani, A. J. In situ observation of faceted growth and morphological instability of a complex-regular eutectic in Zn− Mg− Al system. *Scr. Mater.* **2022**, *206*, 114224.

(28) Lin, Y.-C.; Liu, X.; Chou, K. W.; Tsai, E. H. R.; Zhao, C.; Holler, M.; Diaz, A.; Petrash, S.; Chen-Wiegart, Y.-C. K. Unveiling 3D Morphology of Multiscale Micro-Nanosilver Sintering for Advanced Electronics Manufacturing by Ptychographic X-ray Nanotomography. *Adv. Eng. Mater.* **2020**, *22* (4), 1901250.

(29) Ge, M.; Lee, W.-K. PyXAS−an open-source package for 2D X-ray near-edge spectroscopy analysis. *J. Synchrotron Radiat.* **2020**, *27*, 567−575.

(30) Pattammattel, A.; Tappero, R.; Ge, M.; Chu, Y. S.; Huang, X.; Gao, Y.; Yan, H. High-sensitivity nanoscale chemical imaging with hard x-ray nano-XANES. *Sci. Adv.* **2020**, *6* (37), No. eabb3615.

(31) Manukyan, N.; Martirosyan, V. Investigation of the chlorination mechanism of metal oxides by chlorine. *J. Mater. Process. Technol.* **2003**, *142*, 145−151.

(32) Mayes, R. T.; Kurley, J. M.; Halstenberg, P. W.; McAlister, A.; Sulejmanovic, D.; Raiman, S S.; Dai, S.; Pint, B. *Purification of chloride salts for concentrated solar power applications ORNL/LTR-2018/1052*. Oak Ridge National Lab: Oak Ridge, TN, 2018.

(33) Ge, M.; Coburn, D. S.; Nazaretski, E.; Xu, W.; Gofron, K.; Xu, H.; Yin, Z.; Lee, W.-K. One-minute nano-tomography using hard X-ray full-field transmission microscope. *Appl. Phys. Lett.* **2018**, *113* (8), 083109.

(34) Liu, X.; Bawane, K.; Zheng, X.; Ge, M.; Halstenberg, P.; Maltsev, D. S.; Ivanov, A. S.; Dai, S.; Xiao, X.; Lee, W.-K.; et al. Temperature-Dependent Morphological Evolution during Corrosion of the Ni-20Cr Alloy in Molten Salt Revealed by Multiscale Imaging. *ACS Appl. Mater. Interfaces.* **2023**, *15*, 13772−13782.

(35) Li, L.; Liu, M.; Li, S. Morphology effect on water sorption behavior in a thermoplastic modified epoxy resin system. *Polymer* **2004**, *45*, 2837−2842.

(36) Soles, C. L.; Yee, A. F. A discussion of the molecular mechanisms of moisture transport in epoxy resins. *J. Polym. Sci. Polym. Phys.* **2000**, *38*, 792−802.

(37) Garden, L.; Pethrick, R. A. A dielectric study of water uptake in epoxy resin systems. *J. Appl. Polym. Sci.* **2017**, *134* (16), 44717.

(38) Lide, D. R. *CRC handbook of chemistry and physics*; CRC press, 2004; Vol. *85*.

(39) Gürsoy, D.; De Carlo, F.; Xiao, X.; Jacobsen, C. TomoPy: A framework for the analysis of synchrotron tomographic data. *J. Synchrotron Radiat.* **2014**, *21*, 1188−1193.

(40) Arganda-Carreras, I.; Kaynig, V.; Rueden, C.; Eliceiri, K. W.; Schindelin, J.; Cardona, A.; Sebastian Seung, H. Trainable Weka Segmentation: A machine learning tool for microscopy pixel classification. *Bioinformatics* **2017**, *33*, 2424−2426.

(41) Avery, P.; Genova, A.; McCormick, M.; Chen-Wiegart, Y.-C. K. Combining Interactive and Automatic Volume Registration Techniques in Tomviz. *Microsc. Microanal.* **2024**, *30* (Supplement_1), ozae044.896.

(42) Schwartz, J.; Harris, C.; Pietryga, J.; Zheng, H.; Kumar, P.; Visheratina, A.; Kotov, N. A.; Major, B.; Avery, P.; Ercius, P.; et al. Real-time 3D analysis during electron tomography using tomviz. *Nat. Commun.* **2022**, *13* (1), 4458.

(43) Kirillov, A.; Mintun, E.; Ravi, N.; Mao, H.; Rolland, C.; Gustafson, L.; Xiao, T.; Whitehead, S.; Berg, A. C.; Lo, W.-Y.Segment anything*Proceedings Of The IEEE/CVF International Conference On Computer Vision*IEEEParis, France20234015−4026

(44) Dragonfly *Computer software*; Comet Technologies Canada Inc.: Montreal, Canada, 2020. https://dragonfly.comet.tech/.

(45) Ravel, B.; Newville, M. ATHENA, ARTEMIS, HEPHAESTUS: Data analysis for X-ray absorption spectroscopy using IFEFFIT. *J. Synchrotron Radiat.* **2005**, *12*, 537−541.

(46) Ishitsuka, T.; Nose, K. Solubility study on protective oxide films in molten chlorides created by refuse incineration environment. *Mater. Corros.* **2000**, *51*, 177−181.

(47) Liu, T.; Xu, X.; Liu, W.; Zhuang, X. Corrosion of alloys in high temperature molten-salt heat transfer fluids with air as the cover gas. *Sol. Energy.* **2019**, *191*, 435−448.

(48) Balluffi, R. W.; Allen, S. M.; Carter, W. C. *Kinetics of materials*; John Wiley & Sons, 2005.

(49) Liu, X.; Bawane, K. K.; Clark, C.; Peng, Y.; Woods, M. E.; Halstenberg, P.; Xiao, X.; Lee, W.-K.; Ma, L.; Ehrlich, S. Elucidating the Transition of 3D Morphological Evolution of Binary Alloys in Molten Salts with Metal Ion Additives. *ACS Appl. Mater. Interfaces* **2024**, *16*, 45606−45618.

(50) Gill, S. K.; Sure, J.; Wang, Y.; Layne, B.; He, L.; Mahurin, S.; Wishart, J. F.; Sasaki, K. Investigating corrosion behavior of Ni and Ni-20Cr in molten $ZnCl_2$. *Corros. Sci.* **2021**, *179*, 109105.

(51) Burkhard, W. J.; Corbett, J. D. The Solubility of water in molten mixtures of LiCl and KCl[1]. *J. Am. Chem. Soc.* **1957**, *79*, 6361−6363.

(52) Xie, K.; Kamali, A. R. Electrochemical production of hydrogen in molten salt. *Energy Convers. Manage.* **2022**, *251*, 114980.

(53) Kamali, A. R.; Qiao, D.; Shi, Z.; Wang, D. Green molten salt modification of cobalt oxide for lithium ion battery anode application. *Mater. Chem. Phys.* **2021**, *267*, 124585.

(54) Kamali, A. R. Nanocatalytic conversion of CO_2 into nanodiamonds. *Carbon* **2017**, *123*, 205−215.

(55) Sakamura, Y. Solubility of Li_2O in Molten LiCl−MCl_x (M= Na, K, Cs, Ca, Sr, or Ba) Binary Systems. *J. Electrochem. Soc.* **2010**, *157*, No. E135.

(56) Wang, C.-J.; Li, C.-C. The high-temperature corrosion of austenitic stainless steel with a NaCl deposit at 850 °C. *Oxid. Met.* **2004**, *61*, 485−505.

(57) Lee, J.-W.; Wang, C.-J.; Duh, J.-G. NaCl-induced accelerated oxidation of 304 stainless steel and Fe-Mn-Al alloy at 900 °C. *J. Mater. Sci.* **2003**, *38*, 3619−3628.

(58) Cho, S.-H.; Hong, S.-S.; Kang, D.-S.; Hur, J.-M.; Lee, H.-S. Hot corrosion behavior of Ni-base superalloys in a lithium molten salt. *Met. Mater. Int.* **2009**, *15*, 51−55.

(59) Kracek, F. The binary system Li_2O-SiO_2. *J. Phys. Chem.* **1930**, *34*, 2641−2650.

(60) Ishitsuka, T.; Nose, K. Stability of protective oxide films in waste incineration environment—solubility measurement of oxides in molten chlorides. *Corros. Sci.* **2002**, *44*, 247−263.

(61) Li, Y.; Spiegel, M.; Shimada, S. Corrosion behaviour of various model alloys with NaCl−KCl coating. *Mater. Chem. Phys.* **2005**, *93*, 217−223.

(62) Cho, S.; Zhang, J.; Shin, Y.; Park, S.; Park, H. Corrosion behavior of Fe−Ni−Cr alloys in the molten salt of LiCl−Li_2O at high temperature. *J. Nucl. Mater.* **2004**, *325*, 13−17.

(63) Frangini, S. Corrosion behavior of AISI 316L stainless steel and ODS FeAl aluminide in eutectic $Li_2CO_3-K_2CO_3$ molten carbonates under flowing CO_2-O_2 gas mixtures. *Oxid. Met.* **2000**, *53*, 139−156.